OPEN ACCESS
International Journal of Bifurcation and Chaos, Vol. 31, No. 12 (2021) 2150205 (13 pages)
© The Author(s)
DOI: 10.1142/S0218127421502059

Experimental Evidence of Chaos Generated by a Minimal Universal Oscillator Model

Leonardo Ricci*,†,‡, Alessio Perinelli† and Michele Castelluzzo*
*Department of Physics, University of Trento,
38123 Trento, Italy
†CIMeC, Center for Mind/Brain Sciences,
University of Trento, 38068, Rovereto, Italy
‡leonardo.ricci@unitn.it

Stefano Euzzor and Riccardo Meucci
National Institute of Optics – CNR,
50125 Florence, Italy

Received July 18, 2021

Detection of chaos in experimental data is a crucial issue in nonlinear science. Historically, one of the first evidences of a chaotic behavior in experimental recordings came from laser physics. In a recent work, a Minimal Universal Model of chaos was developed by revisiting the model of laser with feedback, and a first electronic implementation was discussed. Here, we propose an upgraded electronic implementation of the Minimal Universal Model, which allows for a precise and reproducible analysis of the model's parameters space. As a marker of a possible chaotic behavior the variability of the spiking activity that characterizes one of the system's coordinates was used. Relying on a numerical characterization of the relationship between spiking activity and maximum Lyapunov exponent at different parameter combinations, several potentially chaotic settings were selected. The analysis via divergence exponent method of experimental time series acquired by using those settings confirmed a robust chaotic behavior and provided values of the maximum Lyapunov exponent that are in very good agreement with the theoretical predictions. The results of this work further uphold the reliability of the Minimal Universal Model. In addition, the upgraded electronic implementation provides an easily controllable setup that allows for further developments aiming at coupling multiple chaotic systems and investigating synchronization processes.

Keywords: Chaos; nonlinearity; laser; homoclinic bifurcation; chaotic circuit; point processes.

Int. J. Bifurcation Chaos 2021.31. Downloaded from www.worldscientific.com
by 87.5.110.66 on 09/26/21. Re-use and distribution is strictly not permitted, except for Open Access articles.

This is an Open Access article published by World Scientific Publishing Company. It is distributed under the terms of the Creative Commons Attribution 4.0 (CC BY) License which permits use, distribution and reproduction in any medium, provided the original work is properly cited.

Int. J. Bifurcation Chaos 2021.31. Downloaded from www.worldscientific.com
by 87.5.110.66 on 09/26/21. Re-use and distribution is strictly not permitted, except for Open Access articles.

1. Introduction

In a very recent work by Meucci *et al.* [2021], the model of a laser with feedback was revisited by focusing on the minimal nonlinearity necessary to lead to chaos. The model has its origin in laser physics, specifically single-mode CO_2 lasers [Arecchi *et al.*, 1986, 1987], but it can be generalized to describe various physical phenomena, such as neuron dynamics [Guevara *et al.*, 1983; Shastri *et al.*, 2015; Jordi Tiana-Alsina & Masoller, 2019], electronics, opto-electronics and possibly population dynamics [Volterra, 1926, 1931; Lotka, 1910, 1920] and epidemiological models [Schwartz & Smith, 1983]. Therefore, the model makes up a *Minimal Universal Model* for chaos.

The *Minimal Universal Model*, henceforth referred to as μModel, is a three-dimensional model: borrowing from laser terminology, the fastest variable x corresponds to laser intensity, the slowest variable y to population inversion and the intermediate variable z to feedback strength, which acts on an intermediate time scale between x and y. The behavior of the system depends on two main parameters, namely the pump p_0 and the bias B_0. In their work, Meucci *et al.* [2021] provided a thorough analytical study of the system and showed the results of numerical simulations in terms of bifurcation diagrams and phase portraits at a fixed value of p_0 and by changing B_0.

The same work also discusses an experimental implementation in which phase portraits acquired at different operational conditions are described. The evidence of chaos, while convincing due to the similarity with the numerical simulations, was provided at a qualitative level.

Here we discuss a more advanced version of the circuit implementing the μModel, which is similar to the pristine version described by Meucci *et al.* [2021]. As a major experimental improvement, the crucial parameters p_0 and B_0 are set via digital trimmers that allow for a precise and reproducible operation. By exploiting the possibility of remotely controlling the two parameters, the function of the circuit was investigated on a set of 7000 different conditions. In addition, we simulated the system via numerical integration in order to highlight the settings in the parameter space that lead to a chaotic behavior.

By applying a statistical analysis of the inter-spike-intervals (ISIs) we singled out parameter settings that are expected to provide chaos. It is worth mentioning that in many fields ISIs are a important statistic to interpret nonlinear phenomena [Rieke *et al.*, 1997; Richardson *et al.*, 1998; Segundo, 2003; Ricci *et al.*, 2019; Perinelli *et al.*, 2020]. Signals generated by the circuit under the conditions corresponding to these parameter settings were further analyzed by using the divergence rate method [Gao & Zheng, 1993; Rosenstein *et al.*, 1993; Kantz, 1994; Kantz *et al.*, 2013]. Besides providing a clear evidence of chaos, this analysis provides values of the maximum Lyapunov exponent that are in very good agreement with the theoretically and numerically predicted ones.

The present work shows the versatility of the μModel and its experimental implementation: μModel is applicable to a wide range of chaotic phenomena, ranging from lasers to neurons. It is also an ideal candidate to investigate, both from a theoretical and an experimental point of view, synchronization phenomena.

The paper is organized as follows. In Sec. 2, the mathematical aspects of the μModel are summarized. In Sec. 3, we show how to directly design the circuit starting from the very basic equations that describe μModel. Section 4 is devoted to the numerical simulations and to the features that are later used to identify a chaotic behavior. The interpretation of the experimental data and the evidence of chaos are the topic of Sec. 5. Final remarks are presented in Sec. 6.

2. Minimal Universal Model and Circuital Implementation

The dimensionless system of differential equations that define the μModel is:

$$\frac{dx}{d\tau} = -\varepsilon_1 x(1 + k_1 z^2 - p_0 y), \tag{1a}$$

$$\frac{dy}{d\tau} = -y - xy + 1, \tag{1b}$$

$$\frac{dz}{d\tau} = -\varepsilon_2(z - B_0 + B_1 x). \tag{1c}$$

Aiming at an electronic implementation of the system, it is necessary to convert the dimensionless time scale τ in a real time t, and the dimensionless quantities x, y, z appearing in Eqs. (1) in voltages X, Y, Z, respectively.

Starting from time, we set the time constant τ_y that corresponds to the reciprocal of the decay rate

Int. J. Bifurcation Chaos 2021.31. Downloaded from www.worldscientific.com
by 87.5.110.66 on 09/26/21. Re-use and distribution is strictly not permitted, except for Open Access articles.

of the population inversion γ used by Meucci *et al.* [2021]. Consequently:

$$t = \tau_y \cdot \tau.$$

It follows:

$$\frac{dx}{dt} = -\frac{\varepsilon_1}{\tau_y} x(1 + k_1 z^2 - p_0 y),$$

$$\frac{dy}{dt} = -\frac{1}{\tau_y}(y + xy - 1),$$

$$\frac{dz}{dt} = -\frac{\varepsilon_2}{\tau_y}(z - B_0 + B_1 x).$$

We now define

$$\tau_x \equiv \frac{\tau_y}{\varepsilon_1}, \quad \tau_z \equiv \frac{\tau_y}{\varepsilon_2},$$

so that the system of equations becomes:

$$\frac{dx}{dt} = -\frac{1}{\tau_x}(x + k_1 x z^2 - p_0 xy),$$

$$\frac{dy}{dt} = -\frac{1}{\tau_y}(y + xy - 1),$$

$$\frac{dz}{dt} = -\frac{1}{\tau_z}(z - B_0 + B_1 x).$$

In order to linearly map the dimensionless quantities x, y, z into voltages X, Y, Z, a voltage scale is required. Because an electronic implementation of the differential equations requires analog multiplier integrated circuits, the simplest choice for a voltage scale is provided by the "normalization voltage" V_0 used by the analog multipliers (see below), so that:

$$X = V_0 \cdot x, \quad Y = V_0 \cdot y, \quad Z = V_0 \cdot z.$$

It follows:

$$\frac{dX}{dt} = -\frac{1}{\tau_x}\left(X + k_1 \frac{XZ^2}{V_0^2} - p_0 \frac{XY}{V_0}\right), \quad (2a)$$

$$\frac{dY}{dt} = -\frac{1}{\tau_y}\left(Y + \frac{XY}{V_0} - V_0\right), \quad (2b)$$

$$\frac{dZ}{dt} = -\frac{1}{\tau_z}(Z - B_0 V_0 + B_1 X). \quad (2c)$$

The three equations can be electronically emulated by using three inverting, low-pass filters, where the respective time constants τ_x, τ_y, τ_z are set by using suitable RC networks. The inputs to the three filters are the quantities contained in the brackets of the right-hand terms of the previous equations.

The two factors k_1, B_1, which appear in Eqs. (2a) and (2c), respectively, are implementable via resistor ratios. The control parameter B_0, henceforth referred to as "bias" (see [Meucci *et al.*, 2021]), now corresponds to a voltage $B_0 V_0$ that can be straightforwardly provided by using a voltage divider connected with the power supply voltage. Finally, the pump parameter p_0 is also implementable via a resistor ratio. However, this last feature is not desirable from the point of view of an electronic implementation: because p_0 has to be changed, this solution would require a trimmer on the input network of the low-pass filter with output X. A more desirable voltage-controlled implementation is achievable as follows. Let

$$Y' \equiv p_0 \cdot Y.$$

Replacing Y with Y' in the system of Eqs. (2) leads to

$$\frac{dX}{dt} = -\frac{1}{\tau_x}\left(X + k_1 \frac{XZ^2}{V_0^2} - \frac{XY'}{V_0}\right), \quad (3a)$$

$$\frac{dY'}{dt} = -\frac{1}{\tau_y}\left(Y' + \frac{XY'}{V_0} - p_0 V_0\right), \quad (3b)$$

$$\frac{dZ}{dt} = -\frac{1}{\tau_z}(Z - B_0 V_0 + B_1 X). \quad (3c)$$

In this way, the pump p_0 enters the equations — more precisely, the second one — as a constant voltage $p_0 V_0$. By setting:

$$\tau_x = R_1 C_1 \quad \tau_y = R_4 C_2 \quad \tau_z = R_7 C_3,$$

$$\varepsilon_1 = \frac{\tau_y}{\tau_x} = \frac{R_4 C_2}{R_1 C_1} \quad \varepsilon_2 = \frac{\tau_y}{\tau_z} = \frac{R_4 C_2}{R_7 C_3},$$

$$k_1 = \frac{R_1}{R_2} \quad B_1 = \frac{R_7}{R_9},$$

the previous system becomes

$$\frac{dX}{dt} = -\frac{1}{R_1 C_1}\left(X + \frac{R_1}{R_2}\frac{XZ^2}{V_0^2} - \frac{XY'}{V_0}\right), \quad (4a)$$

$$\frac{dY'}{dt} = -\frac{1}{R_4 C_2}\left(Y' + \frac{XY'}{V_0} - p_0 V_0\right), \quad (4b)$$

$$\frac{dZ}{dt} = -\frac{1}{R_7 C_3}\left(Z - B_0 V_0 + \frac{R_7}{R_8} X\right). \quad (4c)$$

Int. J. Bifurcation Chaos 2021.31. Downloaded from www.worldscientific.com
by 87.5.110.66 on 09/26/21. Re-use and distribution is strictly not permitted, except for Open Access articles.

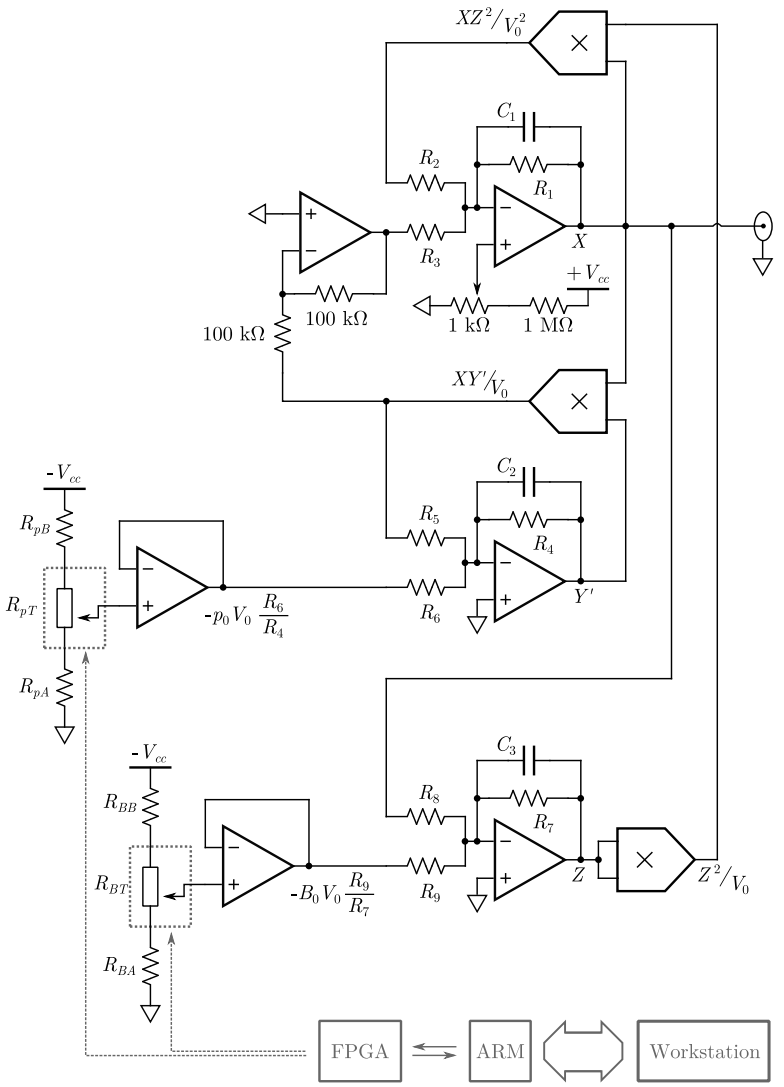

Fig. 1. Schematic of the circuit implementing the μModel. The part containing the three multipliers and the four annex operational amplifiers implements the μModel. The remaining two buffers on the lower left part of the schematic provide the voltages corresponding to the control parameters pump p_0 and bias B_0. The two parameters are varied by acting on the respective digital trimmers R_{pT}, R_{BT}, which are remotely controlled via a board hosting an FPGA and an ARM connected to a workstation via a local network.

The circuit shown in Fig. 1 implements this last system of differential equations. Three operational amplifiers (op-amps; OP07) are used as adders and integrators to produce the three system voltages X, Y, Z. An additional op-amp implements an inverter. Three analog multipliers (AD633JN) are then used to produce the products XY'/V_0, Z^2/V_0, XZ^2/V_0^2. For these components the nominal normalization voltage V_0 is equal to 10 V.

In compliance with the line of action outlined in the work by Meucci *et al.* [2021], we set the fixed parameters ε_1, ε_2, k_1, B_1 and the three time constants τ_x, τ_y, τ_z that appear in Eqs. (3) as reported in Table 1.

A related choice of the discrete capacitive and resistive components that correspond to the parameter settings of Table 1 and to other straightforward circuital constraints — for example, R_3 has to be equal to R_1, and R_5 to R_4 — is reported in Table 2.

Table 1. Fixed parameters entering the system of Eqs. (3).

Parameter	Value	Parameter	Value
ε_1	200	τ_x	49.5 μs
ε_2	10	τ_y	10 ms
k_1	33	τ_z	1 ms
B_1	0.25		

Int. J. Bifurcation Chaos 2021.31. Downloaded from www.worldscientific.com
by 87.5.110.66 on 09/26/21. Re-use and distribution is strictly not permitted, except for Open Access articles.

Table 2. Nominal values of discrete components to yield the parameter settings of Table 1.

Component	Value	Component	Value	Component	Value
C_1	1.5 nF	C_2	1 μF	C_3	100 nF
R_1	33 kΩ	R_4	10 kΩ	R_7	10 kΩ
R_2	1 kΩ	R_5	10 kΩ	R_8	40 kΩ
R_3	33 kΩ	R_6	2 kΩ	R_9	10 kΩ

Table 3. Nominal values of discrete components that are used to set the control parameters p_0 and B_0.

Component	Value	Component	Value
R_{pA}	20 kΩ	R_{BA}	24 kΩ
R_{pT}	10 kΩ	R_{BT}	10 kΩ
R_{pB}	130 kΩ	R_{BB}	510 kΩ

As far as the two control parameters p_0 and B_0 are concerned, their values are set by the trimmers R_{pT}, R_{BT}, respectively, that belong to the voltage dividers in the lower left part of Fig. 1. Let χ_p, χ_B be the fractions, both between 0 and 1, of the trimmer resistances R_{pT}, R_{BT}, respectively. One has:

$$-p_0 V_0 \frac{R_6}{R_4} = -\frac{R_{pA} + \chi_p R_{pT}}{R_{pA} + R_{pT} + R_{pB}} V_{cc},$$

$$-B_0 V_0 \frac{R_9}{R_7} = -\frac{R_{BA} + \chi_B R_{BT}}{R_{BA} + R_{BT} + R_{BB}} V_{cc},$$

where $V_{cc} = 16\,\mathrm{V}$ and all the resistances appearing in the last two expressions are visualized in Fig. 1.

By setting the voltage divider resistances as in Table 3, it follows that

$$p_0 \cong 1.0 + 0.5 \cdot \chi_p, \quad B_0 \cong 0.07 + 0.03 \cdot \chi_B. \tag{5}$$

The two potentiometers R_{pT}, R_{BT} correspond to digitally controlled trimmers (X9C103P). Each trimmer is made up of an array of 99 resistors so that both fractions χ_p, χ_B can take on any value given by $n/99$, with $n = 0, \ldots, 99$. The voltage at each trimmer's wiper is buffered via an op-amp (OP07) and fed to the chaotic circuit.

Finally, it is worth remarking that four resistors in Fig. 1 are unlabeled and directly expressed in terms of their nominal values. Two of these resistors make up the resistive network to yield a unit-gain inverting amplifier that provides the correct sign for the term $-XY'$ in Eq. (3a). The other two resistors, namely a fixed resistor of 1 MΩ and a 1 kΩ trimmer set to $\approx 210\,\Omega$, allow to generate a relatively small, and noncritical, offset ($\sim 3\,\mathrm{mV}$) at the noninverting input of the operational amplifier yielding X. The offset compensates for the spurious bias voltages generated by the different electronic components, which force the X voltage to a stable, negative value. This last condition hampers a correct function of the circuit, which requires $X > 0$.

The whole circuit is mounted on a custom printed circuit board (PCB), as shown in Fig. 2. The circuit is powered by $\pm 16\,\mathrm{V}$ power-supply.

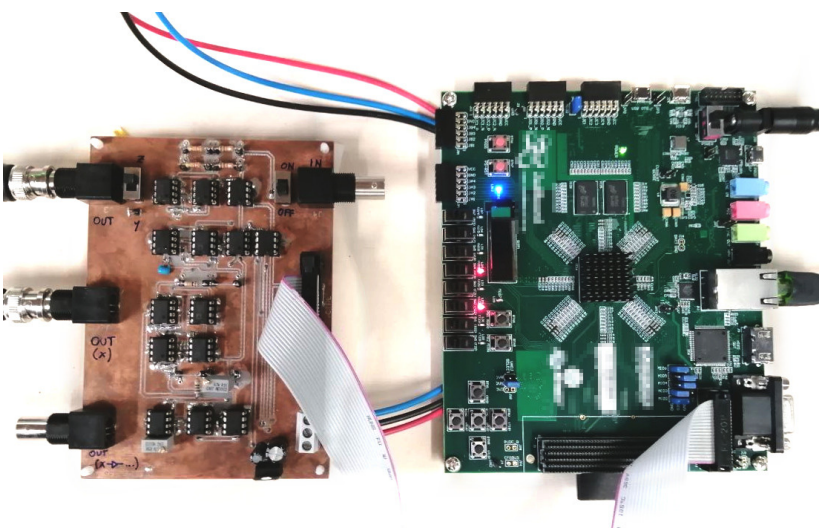

Fig. 2. (Left) PCB hosting the chaotic circuit and the part that relies on the two digital trimmers and delivers voltages proportional to the two control parameters p_0, B_0. The PCB is connected to a power supply and an oscilloscope, both not shown. (Right) Board hosting the FPGA and ARM processors. The board is connected to a second power supply and to a workstation, both not shown. The PCB and the board are connected via a flat cable.

Int. J. Bifurcation Chaos 2021.31. Downloaded from www.worldscientific.com
by 87.5.110.66 on 09/26/21. Re-use and distribution is strictly not permitted, except for Open Access articles.

2.1. *Remote control and acquisition*

The tuning of the parameters p_0, B_0 occurs by acting on the two fractions χ_p, χ_B as follows. The control of each trimmer occurs via LVTTL signals provided by a digital controller implemented on an Avnet Zedboard hosting a Xilinx Zynq-7000 SoC. This device embeds a Field Programmable Gate Array (FPGA) and an ARM processor that runs ArchLinux. A C program running on the ARM processor provides the control interface. The board communicates with a workstation via a local network.

The sampling and acquisition of the signals generated by the system is carried out by a digital oscilloscope Keysight MSO-X 2004A. The instrument is connected via a USB cable for fast data transmission to the same workstation used to control the digital trimmers.

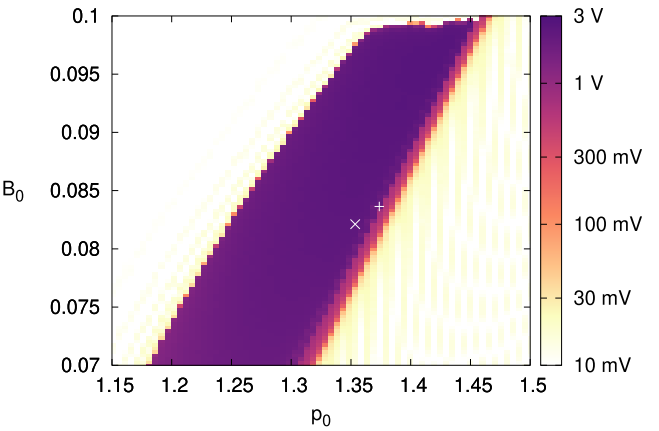

Fig. 3. Map of the averaged AC rms σ_X expressed in V (color scale) for each one of the 7000 pairs of p_0, B_0. For each pair, the average is computed on the related set of ten sampled signals. The white "×" and "+" markers highlight the two pairs whose phase space and time evolutions are displayed in Fig. 4.

3. Experimental Measurements

According to Eqs. (5), p_0 and B_0 can be varied in the ranges $1.00 \leq p_0 \leq 1.50$, $0.07 \leq B_0 \leq 0.10$. However, we found that no oscillation could be observed for $p_0 < 1.15$, i.e. for the lower 30% of the related range. The data acquisition was then set as follows.

The digital trimmer corresponding to p_0 was varied over 70 out of the 100 possible positions, more precisely in the range $\frac{30}{99} \leq \chi_p \leq \frac{99}{99}$ with step $\frac{1}{99}$. Consequently, p_0 varies from 1.152 to 1.500 with step 0.010. For each value of p_0, the digital trimmer corresponding to B_0 was varied over all the available 100 positions, and thus in the range $\frac{0}{99} \leq \chi_B \leq \frac{99}{99}$ with step $\frac{1}{99}$. These settings result in 7000 different pairs of (p_0, B_0). For each pair, a set of ten sampled signals of duration of 1 s each were acquired with a sampling frequency of 62.5 kHz, a voltage full-scale of 13.4 V, and a voltage sensitivity of 4 mV.

In the post-processing phase, given a pair (p_0, B_0) and for each one of the related ten sampled signals, the AC component's root-mean-square voltage (AC rms) corresponding to the voltage standard deviation was computed. This quantity allows for distinguishing stationary points from oscillatory and possibly chaotic behaviors. The map displayed in Fig. 3 shows, for each pair (p_0, B_0), the AC rms σ_X averaged on the related tenfold set.

A map of the kind shown in Fig. 3 cannot distinguish between periodic and chaotic oscillations. To identify a possibly chaotic behavior, one could analyze at least one sampled signal for each one of the 7000 pairs (p_0, B_0) in order to estimate the maximum Lyapunov exponent (MLE) or the correlation dimension [Grassberger & Procaccia, 1983; Perinelli & Ricci, 2018; Perinelli & Ricci, 2020]. However, this approach, besides being definitely demanding from a computational point of view, is not ideal to highlight the physical behavior of the system in the different conditions. For these reasons, we use here a two-step approach: prior to the assessment of the MLE, which makes up the final step, we implement an intermediate one consisting of identifying a limited set of pairs that possibly lead to the generation of chaotic signals.

The identification relies on the comparison of the experimental results and the predictions of numerical simulations in terms of a regularity measure: by exploiting the spiking activity that characterizes the variable x and thus the voltage X of the μModel, we assess the variability of inter-spike-intervals (ISIs). Figure 4 shows two different conditions: in the first one, the phase portrait of the two variables X and Z is a closed orbit, which corresponds to a periodic behavior: the plot of the voltage X versus time shows spikes that occur at a fixed repetition time, and the inter-spike-interval (ISI) does not change. In the second condition, the X–Z phase portrait hints at a possibly chaotic behavior. In this case, the ISIs are not fixed. The standard deviation of the ISIs in the spiking activity of the X voltage therefore makes up a possible indicator of a chaotic dynamics. From the operational point

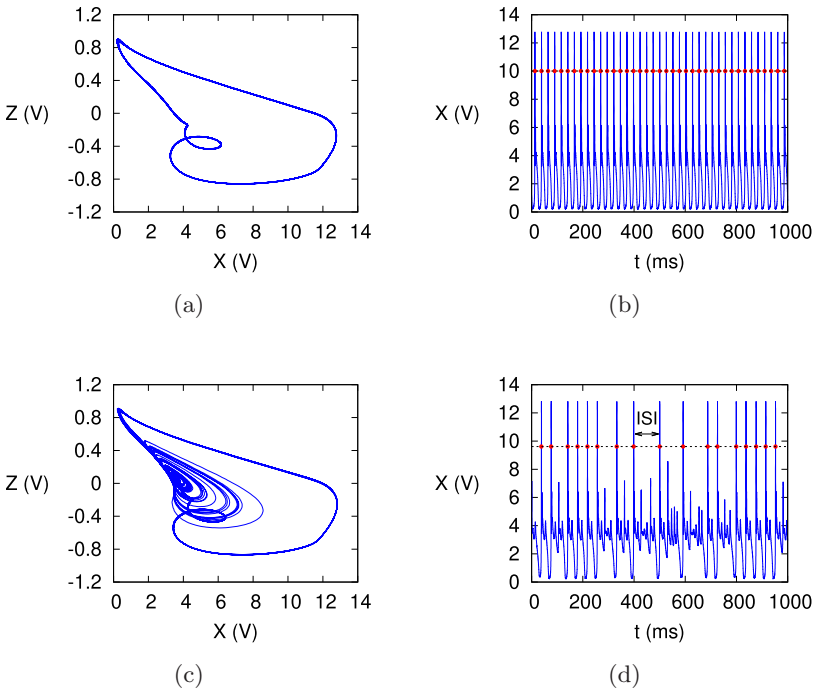

Fig. 4. (a) X–Z phase portrait corresponding to a periodic behavior that was achieved by setting $p_0 = 1.354$, $B_0 = 0.082$; the pair is highlighted in Fig. 3 by the × marker. (b) Graph of the X voltage versus time corresponding to the phase portrait in (a). (c) X–Z phase portrait corresponding to a possibly chaotic behavior that was achieved by setting $p_0 = 1.374$, $B_0 = 0.084$; the pair is highlighted in Fig. 3 by the + marker. The central part of the orbit is characterized by a *twine-ball*-like structure. (d) Graph of the XS voltage versus time corresponding to the phase portrait in (c).

of view, given a sampled signal, spikes are identified by the crossing, on the rising-edge, of a threshold corresponding to 75% of the maximum voltage recorded within that sampled signal.

The next section is devoted to numerical simulations of the μModel and to the relationship between ISI variability and MLE, which makes up the most reliable marker of chaos.

4. Numerical Simulations

In order to interpret the experimental results described in the previous section, numerical simulations of the chaotic system described by the system of Eqs. (1) with the fixed parameters set as in Table 1 were carried out. With regard to the two control parameters p_0, B_0, the same ranges as in the experimental investigations were used.

The integration of differential equations was carried out via a Runge–Kutta Prince–Dormand (8,9) algorithm by randomly setting the starting point. The sampling time was fixed to 10^{-3}, which, due to the time constant τ_y being equal to 10 ms, corresponds to an "experimental" sampling time of 10 μs.

Again, for each pair (p_0, B_0), a set of 10 time series was simulated, each made of $5 \cdot 10^5$ points and thus corresponding to "experimental" time interval of 5 s. The map displayed in Fig. 5 shows, for each pair (p_0, B_0), the AC rms σ_x averaged on the related tenfold set. To allow for a comparison with the experimental results shown in Fig. 3, the σ_x values are multiplied times $V_0 = 10$ V.

A correspondence of the region in which the simulated time series show an oscillation and the region of Fig. 3 in which the AC rms is larger than 0.1 V (i.e. the darker region) is evident. However, the region where the experimental circuit oscillates is definitely larger than the corresponding numerically assessed one. While the deviation of the operational characteristics of the real elements and devices from the ideal and nominal ones is possibly a source of the observed different behavior, a major reason is the sensitivity of the X voltage to noise, as discussed in Sec. 6.

Parallel to the integration of the differential equations, we also numerically estimated the spectrum of Lyapunov exponents by implementing the so-called standard method [Benettin *et al.*, 1980a, 1980b; Skokos, 2010] according to the

Int. J. Bifurcation Chaos 2021.31. Downloaded from www.worldscientific.com
by 87.5.110.66 on 09/26/21. Re-use and distribution is strictly not permitted, except for Open Access articles.

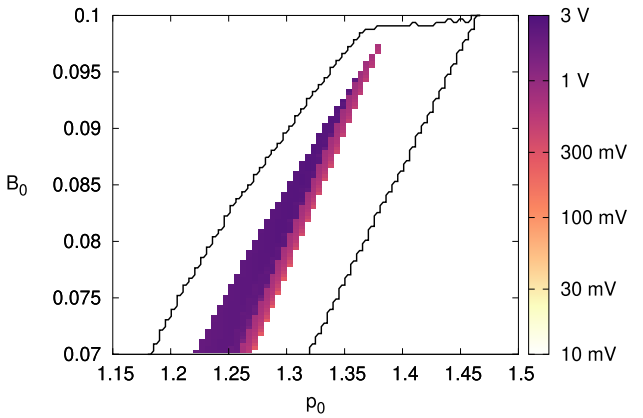

Fig. 5. Map of the averaged AC rms σ_x multiplied times V_0 and thus expressed in V (color scale) for each one of the 7000 pairs of p_0, B_0, in the case of the numerically generated time series. For each pair, the average is computed on the related set of ten simulations. The blank region corresponds to fixed points — reached after a transient time — for which $\sigma_x = 0$. The black contour corresponds to the boundary of the region where the experimental AC rms is larger than 0.1 V (see Fig. 3).

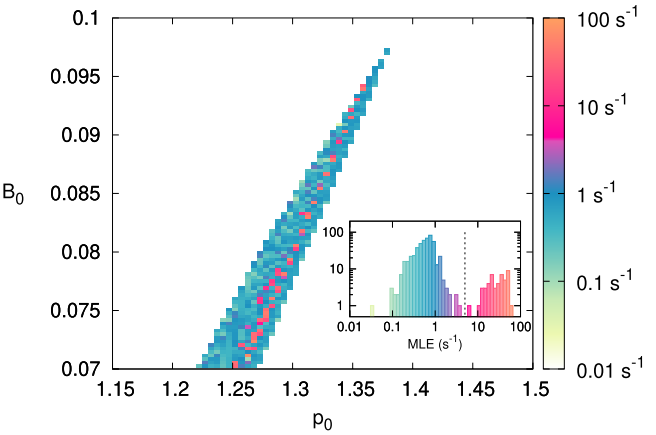

Fig. 6. Map of the averaged numerically assessed MLE expressed in s^{-1} (color scale) for each one of the 7000 pairs of p_0, B_0. For each pair, the average is computed on the related set of ten simulations. Only chaotic pairs, i.e. corresponding to positive MLE values, are plotted. (inset) Histogram of the MLE of the chaotic pairs. The vertical dashed line at MLE $= 5\,s^{-1}$ separates the two parts of the bimodal histogram.

Int. J. Bifurcation Chaos 2021.31. Downloaded from www.worldscientific.com
by 87.5.110.66 on 09/26/21. Re-use and distribution is strictly not permitted, except for Open Access articles.

procedure described in [Franchi & Ricci, 2014]. The spectrum consists of three values, of which only one, namely the MLE, turns out to be positive for a subset of the (p_0, B_0) pairs. Figure 6 shows, only for those values that are positive, the MLE averaged on the related tenfold set. Again, to allow for a comparison with experimental results, the dimensionless MLE value provided by the standard method is divided by $\tau_y = 10\,\text{ms}$. Results are then expressed in s^{-1}.

Henceforth, we refer to a pair (p_0, B_0) that produces a numerically assessed MLE > 0 as a "chaotic pair". The set of chaotic pairs essentially coincides with the set of pairs for which the AC rms takes on the largest values. The inset of Fig. 6 shows the histogram of the positive MLEs. The histogram is clearly bimodal, with most chaotic pairs yielding an MLE $< 5\,s^{-1}$. The maximum MLE value is $66\,s^{-1}$.

In principle, any chaotic pair could be worth considering. However, it is preferable to focus on the pairs that generate higher MLEs, i.e. on those pairs in which chaos is more apparent. In the following, we therefore take into account the pairs for which MLE $> 5\,s^{-1}$ and that are henceforth referred to as "highly-chaotic pairs". Another reason that justifies the choice of a threshold of $5\,s^{-1}$ is that, because the experimentally sampled signals have a duration of 1 s, the threshold approximately corresponds to the smallest value of an MLE detectable by using the divergence exponent algorithm [Gao & Zheng, 1993; Rosenstein *et al.*, 1993; Kantz, 1994; Kantz *et al.*, 2013] that allows to determine the MLE out of an experimentally sampled signal. It is worth noting that the "highly-chaotic" pairs lie along the right side of the triangular region shown in Fig. 6.

Figure 7 shows a scatter plot of the relative ISI standard deviation $s_{\text{ISI}}/\overline{m}_{\text{ISI}}$ as a function of the AC

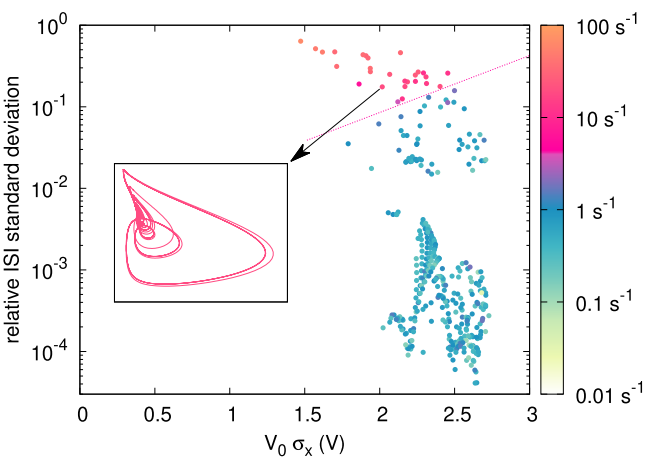

Fig. 7. Scatter plot of the relative ISI standard deviation $s_{\text{ISI}}/\overline{m}_{\text{ISI}}$ as a function of the AC rms $V_0\sigma_x$, in the case of the numerically integrated signals. Each dot corresponds to a chaotic pair. The color of the dot expresses the related MLE via the same palette as in Fig. 6. The red, dashed straight-line separates the highly-chaotic pairs from the other ones and corresponds to the curve of Eq. (6). (inset) X–Z phase portrait corresponding to a possibly chaotic behavior that was achieved by setting $p_0 = 1.333$, $B_0 = 0.088$.

Int. J. Bifurcation Chaos 2021.31. Downloaded from www.worldscientific.com
by 87.5.110.66 on 09/26/21. Re-use and distribution is strictly not permitted, except for Open Access articles.

rms $V_0\sigma_x$ and with each dot being colored according to the related MLE. For each pair, the two statistics $\overline{m}_{\rm ISI}$, $s_{\rm ISI}$ are evaluated as sample mean and sample standard deviation, respectively, on the related set of ten sampled signals. Interestingly, the chaotic pairs having the maximum relative ISI standard deviation do also take on the largest MLE values. More in detail, the highly-chaotic pairs turn out to be located above the separation curve

$$\frac{s_{\rm ISI}}{\overline{m}_{\rm ISI}} = 3.4 \cdot 10^{-3} \cdot 5^{10\sigma_x}. \qquad (6)$$

The shape of the curve, which becomes a straight-line in a log-linear plot as in Fig. 7, as well as the two parameters that define it — namely the factor $3.4 \cdot 10^{-3}$ and the base 5 — were empirically determined. Finally, all chaotic pairs lie in the region defined by $V_0\,\sigma_x > 1\,\mathrm{V}$.

5. Interpretation and Evidence of Chaos in the Experimental Data

The evidence of a set of highly-chaotic pairs that emerges from the numerical simulations can be exploited in the analysis of the experimental data.

Figure 8 shows a scatter plot of the experimental relative ISI standard deviation $s_{\rm ISI}/\overline{m}_{\rm ISI}$ as a function of the AC rms σ_X. While in Fig. 7, the points are approximately uniformly distributed in a region defined by $V_0\,\sigma_x > 1\,\mathrm{V}$, two different point sets are apparent in the experimental case. A leftmost set (blue points) is V-shaped and occurs for $\sigma_X \lesssim 1\,\mathrm{V}$. The analysis of the phase portraits of the signals generated with pairs belonging to this set (see for example the left inset of Fig. 8) suggests an underlying local dynamics emerging after a Hopf bifurcation, as described by Meucci *et al.* [2021]. Also in this case, noise naturally occurring in the experimental implementation is supposed to play a significant role. The remaining, rightmost set (green and orange points) is instead egg-shaped, with most points occurring in the vertical range $10^{-3} \leq s_{\rm ISI}/\overline{m}_{\rm ISI} \leq 10^{-1}$. Comparing the point distribution with the numerically assessed one represented in Fig. 7, a vertical upward compression is evident, which is likely due to the presence of noise in the experimentally sampled signals.

In a crucial step of the present analysis, the egg-shaped set is then divided into two subsets by using the theoretical separation curve expressed by Eq. (6). Within Fig. 8, the experimental points for which $V_0\,\sigma_x > 1\,\mathrm{V}$ and lying above (below) the curve, and thus inside (outside) the numerically assessed, highly-chaotic region, are colored in orange (green), similarly to the numerically assessed points of Fig. 7. Five pairs, labeled from "1" to "5" and belonging to the numerically assessed, highly-chaotic region, were then randomly selected. For the sake of comparison, two additional pairs, labeled "H" (Hopf) and "L" (low MLE), were also selected: "H" lies in the $V_0\,\sigma_x < 1\,\mathrm{V}$ region; "L"

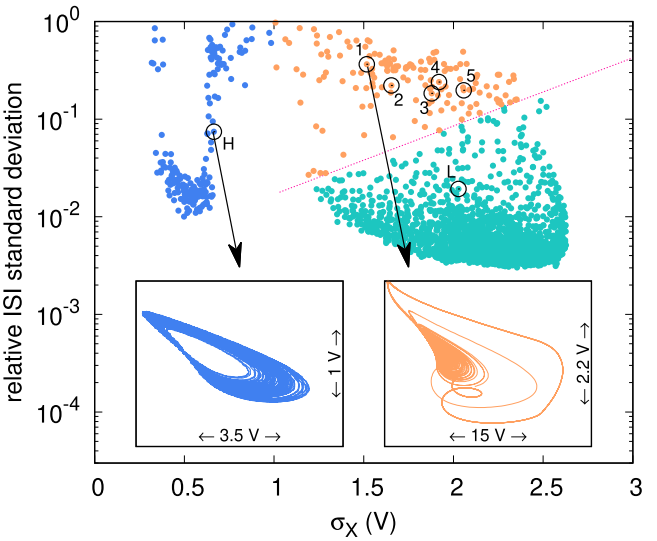

Fig. 8. Scatter plot of the relative ISI standard deviation $s_{\rm ISI}/\overline{m}_{\rm ISI}$ as a function of the AC rms σ_X, in the case of the experimentally sampled signals. Each dot corresponds to a chaotic pair. The colors of the dot are: blue if $V_0\,\sigma_x < 1\,\mathrm{V}$; otherwise, orange (green) if the corresponding pair lies above (below) the separation curve (in fact a straight-line in a log-linear plot) defined by Eq. (6). (left inset) X–Z phase portrait corresponding to the signal acquired by setting the pair to $p_0 = 1.323$, $B_0 = 0.073$ (point "H"). (right inset) X–Z phase portrait corresponding to the signal acquired by setting the pair to $p_0 = 1.414$, $B_0 = 0.092$ (point "1"). Both "H" and "1", along with five additional pairs, namely "2", "3", "4", "5", "L", correspond to the seven pairs reported in Table 4. All these pairs are here marked with a black circle.

Table 4. Coordinates (p_0, B_0) of the seven pairs chosen in the three different regimes identified in Fig. 8.

Label	p_0	B_0
H	1.323	0.073
L	1.323	0.093
1	1.414	0.092
2	1.404	0.099
3	1.363	0.082
4	1.323	0.074
5	1.318	0.092

Int. J. Bifurcation Chaos 2021.31. Downloaded from www.worldscientific.com
by 87.5.110.66 on 09/26/21. Re-use and distribution is strictly not permitted, except for Open Access articles.

has $V_0\,\sigma_x > 1\,\mathrm{V}$ and is located below the separation curve. The coordinates of the seven pairs are reported in Table 4. The pairs are graphically highlighted in Fig. 8.

For each pair, upon accordingly setting the digital trimmers, an additional signal of duration 10 s and sampling frequency 6.25 kHz was acquired. The resulting sequence was then analyzed by implementing the divergence exponent method on a "lattice" of embedding points m, L defined by $2 \leq m \leq 10$, $1 \leq L \leq 10$. Details of the method and its implementation are given in [Ricci *et al.*, 2020]. Here we only mention two main steps, namely the embedding and the divergence exponent evaluations. With regard to the embedding, given a sampled time series $X_n = X(nT)$, where T is the sampling period of 0.16 ms and n runs from 1 to 62 500, and an embedding pair m, L (the embedding dimension and the lag, respectively), the embedded sequence of vectors $\mathbf{Y}_i$ is built by setting the lth component $(0 \leq l \leq m-1)$ of $\mathbf{Y}_i$ to X_{i+lL}, where i runs from 1 to $62\,500 - (m-1)L$. Thereupon, given a delay k, the divergence exponent $\hat{\Lambda}(k)$ is evaluated as:

$$\hat{\Lambda}(k) \equiv \left\langle \log \frac{\|\mathbf{Y}_{i+k} - \mathbf{Y}_{j+k}\|}{\|\mathbf{Y}_i - \mathbf{Y}_j\|} \right\rangle,$$

where the average is computed on a randomly chosen set of "neighboring" embedding vectors $\mathbf{Y}_i$, $\mathbf{Y}_j$, which have to satisfy suitable time and distance constraints [Ricci *et al.*, 2020]. The set size is typically of order 1000.

Figure 9 shows the results for four of the seven chosen pairs. Regardless of the chosen embedding choice, in the case of the points labeled "3", "5", "L", the graph of $\Lambda(k)$ oscillates with a period of about 200, which, because of τ_y, corresponds to a time of several tens ms and thus to a frequency of order 100 Hz. This last value is close to the typical oscillation frequency of the experimentally implemented μModel. In addition, the divergence exponent $\Lambda(k)$ as a function of the delay k shows no statistically reliable region of sustained, i.e. significant, linear growth. The presence of a similar behavior, whose significance is assessed via a procedure relying on a Savitzky–Golay linear filter [Franchi & Ricci, 2014], is crucial: the slope of a significant linear part indeed provides an experimental assessment of MLE. These two facts do not hint at the presence of an underlying chaotic dynamics. With regard to the graphs of $\Lambda(k)$ concerning the pair "H", while no oscillatory behavior appears, a significant linear growth is present only at higher embedding windows. While this could be a marker of an underlying chaotic dynamics — possibly mixed with a noisy one — the fact that the slopes of the linear parts are strongly dependent on the embedding choice do not uphold a similar conclusion.

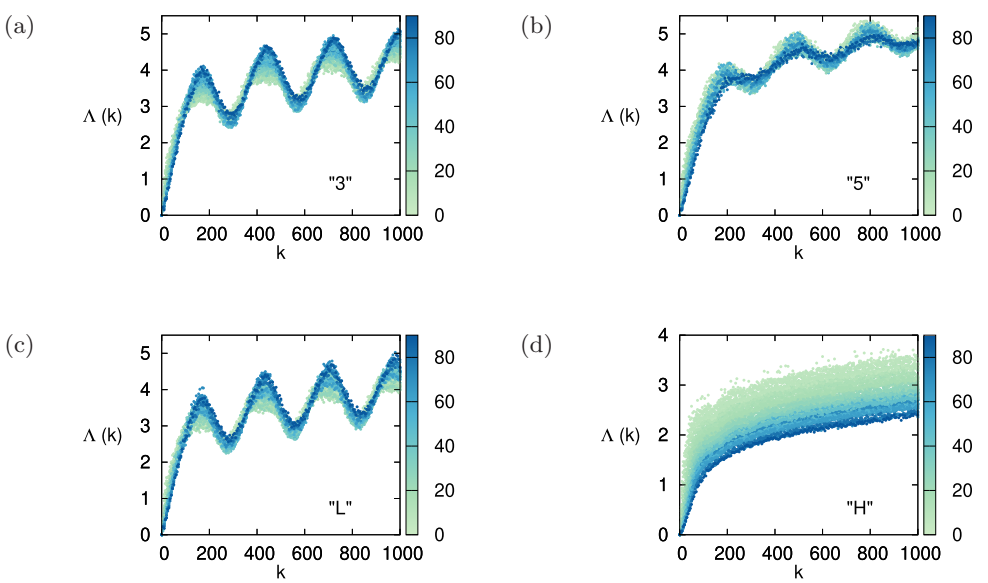

Fig. 9. Graphs of the divergence exponent $\Lambda(k)$ as a function of the delay k evaluated on experimentally sampled signal acquired by setting (p_0, B_0) to the pairs labeled (a) "3", (b) "5", (c) "L", (d) "H", reported in Table 4. In each plot, i.e. for each pair, graphs correspond to different embedding choices. The color scale refers to the embedding window $(m-1)L$.

Int. J. Bifurcation Chaos 2021.31. Downloaded from www.worldscientific.com
by 87.5.110.66 on 09/26/21. Re-use and distribution is strictly not permitted, except for Open Access articles.

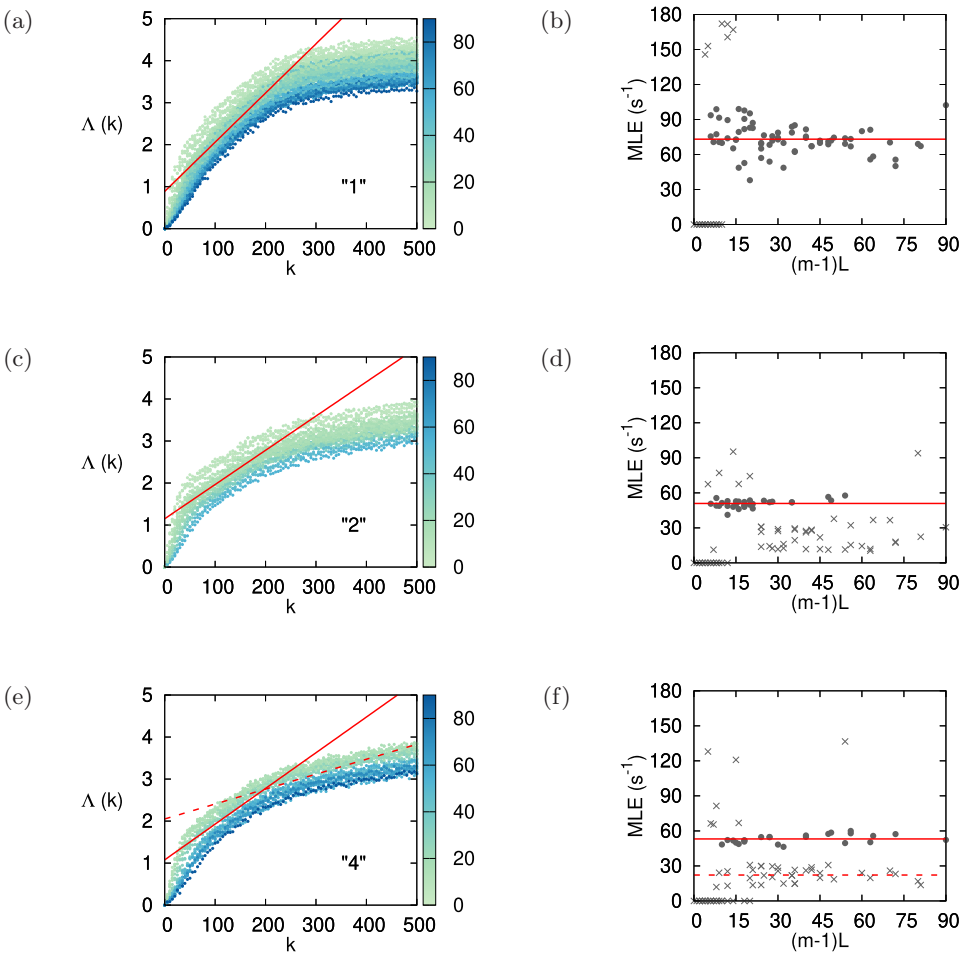

Fig. 10. (Left column) Graphs of the divergence exponent $\Lambda(k)$ as a function of the delay k evaluated on experimentally sampled signal acquired by setting (p_0, B_0) to the pairs labeled (a) "1", (c) "2", (e) "4", reported in Table 4. In each plot, i.e. for each pair, graphs correspond to different embedding. The color scale refers to the embedding window $(m-1)L$. The red, straight lines correspond to the MLE values evaluated in the respective plots on the right column. (Right column) MLE values assessed out of the divergence exponent graphs on the left, and thus in the case of experimentally sampled signal acquired by setting (p_0, B_0) to the pairs labeled (b) "1", (d) "2", (f) "4". The abscissa of the plot is given by the embedding window $(m-1)L$. In the case of "1", the MLE values are clustered at $\approx (70 \pm 20)\,\mathrm{s}^{-1}$, with the average value (red line) at $(73 \pm 13)\,\mathrm{s}^{-1}$. In the case of "2", the MLE values are clustered at $\approx (50 \pm 5)\,\mathrm{s}^{-1}$, with the average value (red line) at $(51 \pm 3)\,\mathrm{s}^{-1}$. In the case of "4", two clusterings appear: at $\approx (20 \pm 5)\,\mathrm{s}^{-1}$ and at $\approx (50 \pm 5)\,\mathrm{s}^{-1}$, thus leading to a more uncertain identification of an underlying chaotic activity. The corresponding two averages are at $(22 \pm 6)\,\mathrm{s}^{-1}$ (red dashed line) and at $(53 \pm 4)\,\mathrm{s}^{-1}$ (red line), respectively.

Figure 10 shows the results for the three remaining pairs, namely "1", "2", "4". In the graphs of $\Lambda(k)$ of all three cases no oscillatory behavior appears. In addition, a significant linear growth is present, which is approximately constant at different embedding dimensions. As shown in Fig. 10(b), this fact is particularly clear in the condition defined by the pair "1": the slopes of the linear parts are mostly clustered between $30\,\mathrm{s}^{-1}$ and $90\,\mathrm{s}^{-1}$. An average on this set provides a value of $(73 \pm 13)\,\mathrm{s}^{-1}$. With regard to the pair "2", the slopes make a cluster at about $50\,\mathrm{s}^{-1}$. Finally, in the case of the pair "4", a clustering appears again at about $50\,\mathrm{s}^{-1}$ and possibly also at about $20\,\mathrm{s}^{-1}$, leading to a more uncertain identification of an underlying chaotic behavior than in the two previous cases. In all three cases the values of the MLE are statistically compatible with the range $(10 \div 66)\,\mathrm{s}^{-1}$ evaluated via the theory and the numerical simulations.

As a final analysis, Fig. 11 shows the map of the relative ISI standard deviation $s_{\mathrm{ISI}}/\overline{m}_{\mathrm{ISI}}$ evaluated for each pair (p_0, B_0) on the related set of ten sampled signals. The pairs belonging to the numerically assessed, highly-chaotic region of Fig. 8, where

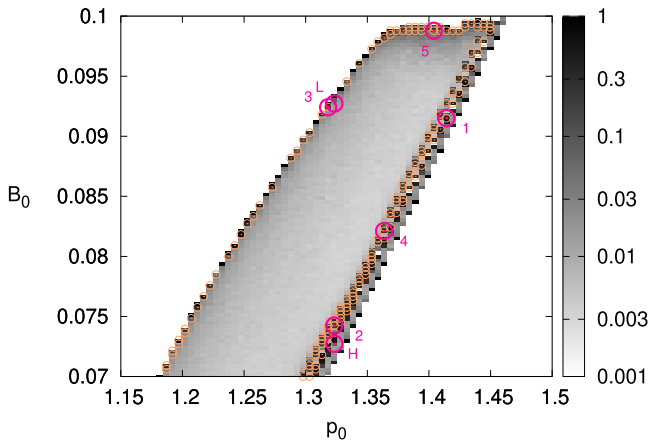

Fig. 11. Map of the relative ISI standard deviation $s_{\mathrm{ISI}}/\overline{m}_{\mathrm{ISI}}$ (color scale) for each one of the 7000 pairs of p_0, B_0 for which $\sigma_X \geq 10\,\mathrm{mV}$. The points marked with an orange circle correspond to the orange points of Fig. 8. The seven points reported in Table 4 are marked with magenta circles and labeled accordingly.

they are colored in orange, are accordingly marked with orange circles in Fig. 11. Interestingly, those pairs turn out to be located on the boundary of the wing-shaped region that contains the pairs with $\sigma_X \geq 10\,\mathrm{mV}$, i.e. the pairs for which an oscillation occurs. Moreover, the three pairs "1", "2", "4" that show a chaotic behavior lie on the lower part of the wing-shaped region, i.e. in a position very similar to that of the higher-MLE pairs resulting from the numerical analysis and appearing in Fig. 6.

6. Discussion

The experimental investigation and the numerical simulations described above uphold and expand what was described in the pristine work on μModel and its experimental implementation [Meucci *et al.*, 2021].

The main conclusion that can be drawn is that the μModel works in a very reliable way. Choices of the parameter pair (p_0, B_0) that lead to time series characterized by a relatively high variability of the relative ISI standard deviation correspond to a robust chaotic behavior. Nevertheless, there are several aspects that need a deeper analysis, both from the theoretical and the experimental points of view. These aspects can explain the discrepancies between the experimental model and the theoretical one.

The first problem is the sensitivity of the X voltage to noise. By considering the experimental implementation described in this work, the theory predicts this quantity to remain in the range of μV for a significant part of a cycle. On the other hand, these voltage values are comparable to voltage contributions due to noise, which can lead to a "rebound" of the X variable prior to what would be expected in an ideal situation. While this aspect could be exploited in order to develop a noise sensor, it deserves further investigation in order to precisely assess the effect of noise on the μModel dynamics.

Similar considerations underlie the second problem, which also mainly concerns the X variable, namely the sensitivity to bias. For example, bias can enter the X evolution as noise affecting the variable Z, which appears in the equation of dX/dt as a square, thus producing a positive, i.e. biased, contribution.

However, it is a matter of fact that the two problems outlined here only marginally affect the chaotic behavior of the circuit. This fact can be explained by observing that, first, the chaotic dynamics becomes dominant only in a *twine-ball*-like region [see Fig. 4(c)] of the attractor, which is characterized by values of Z close to zero and by values of X close to the midpoint of its range. Second, the regions in which X approaches its minimum value are characterized by a very regular behavior that in no case — i.e. even when the dynamics is indeed chaotic — contributes to chaos.

A third and final point that one has to cope with is the finite bandwidth of the ICs used in the experimental implementation. For example, the numerical integrations of Eqs. (1) provide maximum values of the dimensionless variable x of about 3. These values would correspond to experimental values of 30 V. However, we observed maximum values of about 13 V, which is well below the saturation voltage of the ICs. The discrepancy is mainly due to the finite gain-bandwidth product of the op-amp whose output corresponds to X and whose surrounding network provides a filter with a low-frequency gain of 33. Again, this aspect does not influence the chaotic behavior of the system due to the regular behavior that characterizes the sections of the trajectory in the phase space that correspond to the spikes of X.

In conclusion, while the issues outlined above require further investigations, μModel provides a promising model to explore chaotic dynamics in an experimental context. Its operational robustness makes it an ideal candidate to explore

Int. J. Bifurcation Chaos 2021.31. Downloaded from www.worldscientific.com
by 87.5.110.66 on 09/26/21. Re-use and distribution is strictly not permitted, except for Open Access articles.

synchronization effects between two or more oscillators [Minati *et al.*, 2019].

References

Arecchi, F. T., Gadomski, W. & Meucci, R. [1986] "Generation of chaotic dynamics by feedback on a laser," *Phys. Rev. A* **34**, 1617–1620.

Arecchi, F. T., Meucci, R. & Gadomski, W. [1987] "Laser dynamics with competing instabilities," *Phys. Rev. Lett.* **58**, 2205–2208.

Benettin, G., Galgani, L., Giorgilli, A. & Strelcyn, J. M. [1980a] "Lyapunov characteristic exponents for smooth dynamical systems and for Hamiltonian systems; a method for computing all of them. Part 1: Theory," *Meccanica* **15**, 9–20.

Benettin, G., Galgani, L., Giorgilli, A. & Strelcyn, J. M. [1980b] "Lyapunov characteristic exponents for smooth dynamical systems and for Hamiltonian systems; a method for computing all of them. Part 2: Numerical application," *Meccanica* **15**, 21–30.

Franchi, M. & Ricci, L. [2014] "Statistical properties of the maximum Lyapunov exponent calculated via the divergence rate method," *Phys. Rev. E* **90**, 062920.

Gao, J. & Zheng, Z. [1993] "Local exponential divergence plot and optimal embedding of a chaotic time-series," *Phys. Lett. A* **181**, 153–158.

Grassberger, P. & Procaccia, I. [1983] "Characterization of strange attractors," *Phys. Rev. Lett.* **50**, 346–349.

Guevara, M. R., Glass, L., Mackey, M. C. & Shrier, A. [1983] "Chaos in neurobiology," *IEEE Trans. Syst. Man Cybern.* **SMC-13**, 790–798.

Jordi Tiana-Alsina, C. Q. & Masoller, C. [2019] "Comparing the dynamics of periodically forced lasers and neurons," *New J. Phys.* **21**, 103039.

Kantz, H. [1994] "A robust method to estimate the maximal Lyapunov exponent of a time series," *Phys. Lett. A* **185**, 77–87.

Kantz, H., Radons, G. & Yang, H. [2013] "The problem of spurious Lyapunov exponents in time series analysis and its solution by covariant Lyapunov vectors," *J. Phys. A*: *Math. Theor.* **46**, 254009-1–24.

Lotka, A. J. [1910] "Contribution to the theory of periodic reaction," *J. Phys. Chem.* **14**, 271–274.

Lotka, A. J. [1920] "Analytical note on certain rhythmic relations in organic systems," *Proc. Natl. Acad. Sci. USA* **6**, 410–415.

Meucci, R., Euzzor, S., Arecchi, F. T. & Ginoux, J. [2021] "Minimal universal model for chaos in laser with feedback," *Int. J. Bifurcation and Chaos* **31**, 2130013-1–10.

Minati, L., Ito, H., Perinelli, A., Ricci, L., Faes, L., Yoshimura, N., Koike, Y. & Frasca, M. [2019] "Connectivity influences on nonlinear dynamics in weakly-synchronized networks: Insights from Rössler systems, electronic chaotic oscillators, model and biological neurons," *IEEE Access* **7**, 174793.

Perinelli, A. & Ricci, L. [2018] "Identification of suitable embedding dimensions and lags for time series generated by chaotic, finite-dimensional systems," *Phys. Rev. E* **98**, 052226.

Perinelli, A. & Ricci, L. [2020] "Chasing chaos by improved identification of suitable embedding dimensions and lags," *Chaos* **30**, 123104.

Perinelli, A., Castelluzzo, M., Minati, L. & Ricci, L. [2020] "SpiSeMe: A multi-language package for spike train surrogate generation," *Chaos* **30**, 073120.

Ricci, L., Castelluzzo, M., Minati, L. & Perinelli, A. [2019] "Generation of surrogate event sequences via joint distribution of successive inter-event intervals," *Chaos* **29**, 121102.

Ricci, L., Perinelli, A. & Franchi, M. [2020] "Asymptotic behavior of the time-dependent divergence exponent," *Phys. Rev. E* **101**, 042211.

Richardson, K. A., Imhoff, T. T., Grigg, P. & Collins, J. J. [1998] "Encoding chaos in neural spike trains," *Phys. Rev. Lett.* **80**, 2485–2488.

Rieke, F., Warland, D., de Ruyter van Steveninck, R. & Bialek, W. [1997] *Spikes*: *Exploring the Neural Code* (MIT Press, Cambridge, MA).

Rosenstein, M., Collins, J. & Luca, C. D. [1993] "A practical method for calculating largest Lyapunov exponents from small data sets," *Physica D* **65**, 117–134.

Schwartz, I. B. & Smith, H. [1983] "Infinite subharmonic bifurcation in an SEIR epidemic model," *J. Math. Biol.* **18**, 233–253.

Segundo, J. P. [2003] "Nonlinear dynamics of point process systems and data," *Int. J. Bifurcation and Chaos* **13**, 2035–2116.

Shastri, B. J., Nahmias, M. A., Tait, A. N., Wu, B. & Prucnal, P. R. [2015] "SIMPEL: Circuit model for photonic spike processing laser neurons," *Opt. Express* **23**, 8029–8044.

Skokos, C. [2010] "The Lyapunov characteristic exponents and their computation," *Lect. Notes Phys.* **790**, 63–135.

Volterra, V. [1926] "Variazioni e fluttuazioni del numero d'individui in specie animali conviventi," *Mem. Acad. Lincei Roma* **2**, 31–113.

Volterra, V. [1931] *Variations and Fluctuations of the Number of Individuals in Animal Species Living Together* (McGraw-Hill, NY, USA), pp. 409–448.

Int. J. Bifurcation Chaos 2021.31. Downloaded from www.worldscientific.com
by 87.5.110.66 on 09/26/21. Re-use and distribution is strictly not permitted, except for Open Access articles.